ADVANCED ENERGY & SUSTAINABILITY RESEARCH
www.advenergysustres.com

Exploring Salinity Gradient Power in Sweden: Key Factors, Machine Learning Predictive Modeling, and Life Cycle Assessment

Younes Mohammadi, Mehzabeen Mannan, Sara Fazeli, Noor Ul Afsar, Venkata K. K. Upadhyayula, and Naser Tavajohi**

This study explores strategies to maximize salinity gradient power (SGP) generation using reverse electrodialysis (RED), focusing on key operating parameters under Swedish environmental conditions. Herein, using a full-factorial experimental design, seawater salinity, flow velocities, and water temperature is varied across three levels to assess their impact on SGP output. machine learning methods predict power density (*PD*), including 1) ensemble learning with decision tree (DT), 2) gaussian process regression (GPR), and 3) artificial neural network (ANN). Fivefold cross-validation confirms the ANN's high accuracy (root mean squared error (RMSE): 1.173%, R^2: 99.35%), closely followed by GPR (RMSE: 1.95%, R^2: 99.17%). A feature and trend pattern analysis among the input factors reveals sea salinity as the primary influence on *PD*, with temperature as the secondary contributor. Complementing this, a life cycle assessment examines the environmental impact of RED systems, identifying the Seawater River RED and brine-wastewater treatment plant RED systems as having environmental effects, particularly on ozone layer depletion and freshwater toxicity. Carbon fiber-based (CF) electrodes, especially lignin CF, demonstrate a lower impact, yet concerns remain over key sustainability challenges. These findings highlight SGP's potential as a viable renewable source, highlighting areas for future material selection and system efficiency improvements.

1. Introduction

Since the industrial revolution, energy demand has surged, leading to substantial greenhouse gas emissions, which in turn have resulted in climate change.[1–3] Projections estimate that by 2035, greenhouse gas emissions will range 19 billion tons of carbon dioxide equivalent (BtCO2eq) globally, with yearly growth rates of 2.39% and 1.71%, respectively.[4] In efforts to protect the environment and reduce carbon emissions, extensive research has been focused on harnessing clean and renewable energy resources (RERs) like ocean, wind, biomass, and solar energies to promote the sustainable progress of modern society.[5–7] Among these, wind and solar energy have emerged as the most economical renewable options.[8–10] Nevertheless, their intermittent nature poses challenges, limiting the potential for completely replacing fossil fuel consumption. In this scenario, salinity gradient power/energy (SGP/SGE), also known as Blue Energy, seems like an attractive option. Blue energy is considered a clean and environmentally friendly energy source that can be exploited continuously 24 h per day and 365 days a year. SGP relies on the difference in salinity of water resources to generate

Y. Mohammadi
Department of Applied Physics and Electronics
Umeå University
90187 Umeå, Sweden

M. Mannan
Department of Civil and Environmental Engineering
South Dakota School of Mines and Technology
501 E Saint Joseph Blvd, Rapid 57701, SD, USA

The ORCID identification number(s) for the author(s) of this article can be found under https://doi.org/10.1002/aesr.202500124.

DOI: 10.1002/aesr.202500124

S. Fazeli
Groupe de Recherches surl'Energétique des Milieux Ionisés – GREMI
University de Orléans
45067 Orleans, France

N. Ul Afsar, V. K. K. Upadhyayula, N. Tavajohi
Department of Chemistry
Umeå University
90187 Umeå, Sweden
E-mail: krishna.upadhyayula@umu.se; naser.tavajohi@umu.se

power without noticeable greenhouse gas emissions. In addition to anthropogenic resources such as desalination plants and wastewater treatment plants, natural resources such as river mouths, where freshwater meets saline seawater, present prime locations for SGE extraction due to the readily available salinity gradients.[11,12]

Research conducted in 1973 evaluated the global potential of SGP at river mouths, revealing an astonishing potential output of 1.4–2.6 TWh worldwide.[13] The following studies refined these estimates, suggesting a theoretical power potential of 1.724–3.158 TW from river mouth systems, which is equivalent to 15 102–27 664 TWh.[14,15] This amount of energy is roughly equivalent to the global electricity usage in 2011, which was around 20 407 TWh.[13] Nevertheless, real-world factors such as location, extraction efficiency (0.2), operational efficiency (0.84), and technological efficiency reduce the practical SGE potential significantly. For instance, a study of river-sea mixing showed a revised estimate of 625 TWh $year^{-1}$.[13] Despite the discrepancy in the total available energy for harnessing, the amount of energy available is significant enough that this renewable energy source should not be overlooked. Therefore, regional and local-scale assessments of the potential for SGE have been conducted in several countries. Notable examples include the Great Salt Lake and the Columbia river in the United States,[16] the Rhine and Meuse rivers in the Netherlands,[17] the Paraná River in Argentina, the Amazon River in Brazil, the Congo River spanning the Congo and Angola,[16] and the dead sea[18] as well as studies in Australia,[19] Canada,[20] and Norway.[17] countries such as Italy, Japan, South Korea, Singapore, Denmark, and the Netherlands have conducted pilot-scale projects for harvesting SGP. Some of these pilot sites, including those in Italy and the Netherlands, are still operational, while others, such as Statkraft in Norway, have been discontinued. Meanwhile, a paper published in 2024 critically assessed the competitiveness of SGP.[21]

Despite being an interesting energy source based on theoretical estimates, the high technological costs of blue energy limit its application, and the environmental impacts of existing technologies are not fully recognized.[22] These limitations necessitate further studies to understand and optimize operating conditions, potentially decrease the cost of energy production, and assess the life cycle of the technologies to recognize their potential impacts on humans and the environment.

Among the different technologies for harvesting blue energy, reverse electrodialysis (RED), which is a membrane-based technology, is a promising candidate for large-scale implementation.[23] RED generates electricity from the salinity gradient between saline solutions (e.g., seawater) and dilute solutions (e.g., freshwater) by using alternating cation-exchange membranes (CEM) and anion-exchange membranes (AEM). When saline and dilute solutions are placed on opposite sides of the membrane stack, cations (such as sodium) from the saline solution flow through the CEM toward the dilute solution, while anions, such as chloride, move through the AEM in the opposite direction. This ion movement creates an electrochemical potential and generates a voltage difference across the membranes, which can be harnessed by connecting electrodes to the system, thereby producing electrical power.[24–27]

The potential for SGP across various geographical regions in a country like Sweden is significantly influenced by environmental factors, including salinity levels, temperature variations, and flow rates of water bodies. A comprehensive assessment of these operating conditions is essential, as it provides valuable insights into how geographical and seasonal fluctuations affect the operating parameters and overall performance of RED. Such evaluations not only facilitate the development of targeted optimization strategies but also contribute to cost-reduction efforts in the implementation of SGE technologies. Therefore, the first part of this study investigates the production of blue energy over a range of salinity, temperature, and flow rates, considering Sweden's seasonal and geographical contexts as an exemplary case study. Following that, artificial intelligence algorithms, in particular machine learning (ML) and artificial neural networks (ANNs), were used to analyze the influence of seasonal and geographical variations on the performance of RED by estimation of SGP utilizing a linear or nonlinear relationship between seawater salinity, and its controlling factors, such as temperature and river discharge.

As stated in published studies on SGP, this energy source is generally regarded as having a low environmental impact, and this property has been considered as an advantage.[28–30] In this context, the life cycle assessment (LCA) methodology provides a robust framework for evaluating the impacts of SGP on human health and the environment. LCA allows a comprehensive analysis of the environmental effects associated with the entire life cycle of systems such as RED, including phases such as production, transportation, installation, operation, and waste management. Additionally, it enables comparisons of these results with those from other renewable energy technologies, such as solar and wind power 54. In 2020, C. Tristan et al. assessed the environmental impact of SGE technology, specifically RED, focusing on two scenarios: a standalone RED unit and an integrated RED-Sea Water Reverse Osmosis system. The results of these studies reveal that SGE-RED technology can be environmentally competitive with other renewable energy sources, such as solar and wind power, especially when scaled up.[31] Another study published in 2021 found that a well-designed SGE plant can minimize environmental impact, support local ecotourism, aid ecosystem conservation, and contribute to clean and renewable energy.[32]

It is important to note that the environmental impact of harvesting technologies, such as RED, can be significantly influenced by the components used in the RED system (e.g., spacers, membrane materials, electrodes), a factor that has been overlooked in past years. Therefore, the second part of this manuscript will focus on the LCA of RED, with a specific emphasis on its components. More specifically, this study assesses how changes in electrode type impact the overall environmental performance of the system, allowing for a more comprehensive understanding of potential improvements and trade-offs in the RED technology.

2. Experimental Section

2.1. Materials

Sodium chloride (NaCl), magnesium chloride ($MgCl_2$), sodium sulfate (Na_2SO_4), calcium chloride ($CaCl_2$), potassium chloride (KCl), sodium bicarbonate ($NaHCO_3$), potassium bromide (KBr), boric acid (H_3BO_3), strontium chloride ($SrCl_2$), and

sodium fluoride (NaF) were purchased from Sigma-Aldrich. The sodium bicarbonate ($NaHCO_3$) was purchased from Carlo Erba Reagents. All of the above chemicals were used to prepare a simulated seawater (SSW) composition according to the ASTM D1141-98 standard, as shown in **Table 1**, which mimics the composition of the water in the Baltic Sea.

Potassium ferrocyanide ($K_4[Fe(CN)_6]$), potassium ferricyanide ($K_3[Fe(CN)_6]$) were purchased from Sigma-Aldrich, and NaCl was used to prepare the electrode rinsing solution (electrolyte solutions). The electrolyte solution composition was 0.05 M $K_4[Fe(CN)_6]$ and $K_3[Fe(CN)_6]$ and 0.25 M NaCl. A standard range of CEM (code: PC SK) and AEM (code: PC SA) from Pccell (Germany) was used. Their characteristics are shown in **Table 2**.

2.2. Experiment

The experimental setup comprised the bench-scale RED apparatus, the membrane stack, a resistive box, and three tanks, each linked to independent circulating pumps. A schematic drawing of the RED system is shown in **Figure 1**a. In the setup, seawater salinity (high concentration, HC) and river concentration (low concentration, LC) solutions were kept in two of the 10 L tanks. The temperature of the tanks was controlled by an external heater/cooler. As shown in Figure 1b, the RED setup employs both AEMs and CEMs, arranged in alternating layers. Spacers were used to maintain proper spacing between the membranes and to create compartments for the feed solutions. During operation, the dilute solutions (LC) and the concentrated solutions (HC) flowed alternately through the compartments. Salt transport from the concentrate to the dilute compartments occured due to the concentration gradient. As a result, an ionic current was generated through the stack, which was finally converted into an electric current utilizing a redox reaction at the electrodes. The negatively charged ions in the anolyte solution lost electrons at the anode, a ruthenium-iridium-coated titanium mesh type. These electrons flowed through an external circuit at the cathode, which was also a ruthenium-iridium-coated titanium mesh type. At the same time, positively charged ions from the catholyte solution gained electrons at the cathode. The following reactions occur during this entire process:

$$\text{Anode:}\quad K_4[Fe(CN)_6] \rightarrow K_3[Fe(CN)_6] + e^- \tag{1}$$

$$\text{Cathode:}\quad K_3[Fe(CN)_6] + e^- \rightarrow K_4[Fe(CN)_6] \tag{2}$$

During the experiment, the effects of various operating parameters on the performance of a RED setup were analyzed. Specifically, the effects of HC solution concentration, temperature, and flow rate of both HC and LC solutions were investigated. The concentration of the LC solution was kept constant at 0.005 M. The RED's external resistance box was used to vary the resistance and were performed experiments at various resistances, including 80, 20, 5, and 2 ohms. The experiments were repeated to observe the effects of temperature and flow rate at three different values for each concentration level (high, medium, and low) (see **Table 3**). During the experiments, the voltages were measured. These values were then used for the calculation of current density and power density (PD).

The HC and LC flow velocities were determined based on the Swedish water resources. Sea salinity (i.e., HC) was also measured in grams per liter ($g\,L^{-1}$), ranging from 2.5 $g\,L^{-1}$ at the lowest level, characteristic of northern coastal areas in Sweden, to 17.5 $g\,L^{-1}$ at the intermediate level, typical of central coastal regions, and finally, to 32.5 $g\,L^{-1}$ at the highest level, typical of southern coastal areas in Sweden (see Figure 1c,d).

A total of 81 experiments were conducted, each with varying salt concentrations. Specifically, 27 experiments utilized a 2.5 $g\,L^{-1}$ salt solution, followed by another 27 with 17.5 $g\,L^{-1}$, and the remaining 27 with 32.5 $g\,L^{-1}$. This sequential approach aligned with the concept of a full factorial experimental design, where each of the four factors, each with three levels (Low, Medium, and High), necessitates $3^4 = 81$ experiments. During all 81 experiments, the voltage values were measured. These values were then used to calculate current density and *PD*. Based on the experimental data, the performance of a RED stack can be expressed for the relations between voltage (V), current (I), and power (P) shown in Equation (3).

Table 1. Composition of SSW based on ASTM D1141-98 standard (ASTM standard for standard practice for the preparation of substitute Ocean Water, Designation: D 1141-98 (Reapproved 2003), ASTM International, United States of America).

Salt	Composition [wt%]	2.0 [$g\,L^{-1}$]	17.50 [$g\,L^{-1}$]	32.50 [$g\,L^{-1}$]
Sodium chloride	58.49	1.4623	10.2358	19.0093
Magnesium chloride	26.46	0.6615	4.6305	8.5995
Sodium sulfate	9.75	0.2438	1.7063	3.1688
Calcium chloride	2.765	0.0691	0.4839	0.8986
Potassium chloride	1.645	0.0411	0.2879	0.5346
Sodium bicarbonate	0.477	0.0119	0.0835	0.1550
Potassium bromide	0.238	0.0060	0.0417	0.0774
Boric acid	0.071	0.0018	0.0124	0.0231
Strontium chloride	0.095	0.0024	0.0166	0.0309
Sodium fluoride	0.007	0.0002	0.0012	0.0023

Table 2. Properties of the membranes used in the RED stack.

Membrane	PC SA	PC SK
General use	Standard	Standard
Type of membrane	Anionic	Cathionic
Ionic transfer capacity	>0.95	>0.95
Resistivity coefficient	≈1.8	≈2.5
Water content [%w]	≈14	≈9
Ion exchange capacity:		
Strong base [meq g^{-1}]	≈1.2	3
Weak base [meq g^{-1}]	≈0.7	n/a
Maximum temperature [°C]	60	50
Stability Ph	0 to 9	0 to 11
Thickness [µm]	100 to 110	
Reinforcement	Polyester	
Ionic form	Cl^-	Na^+

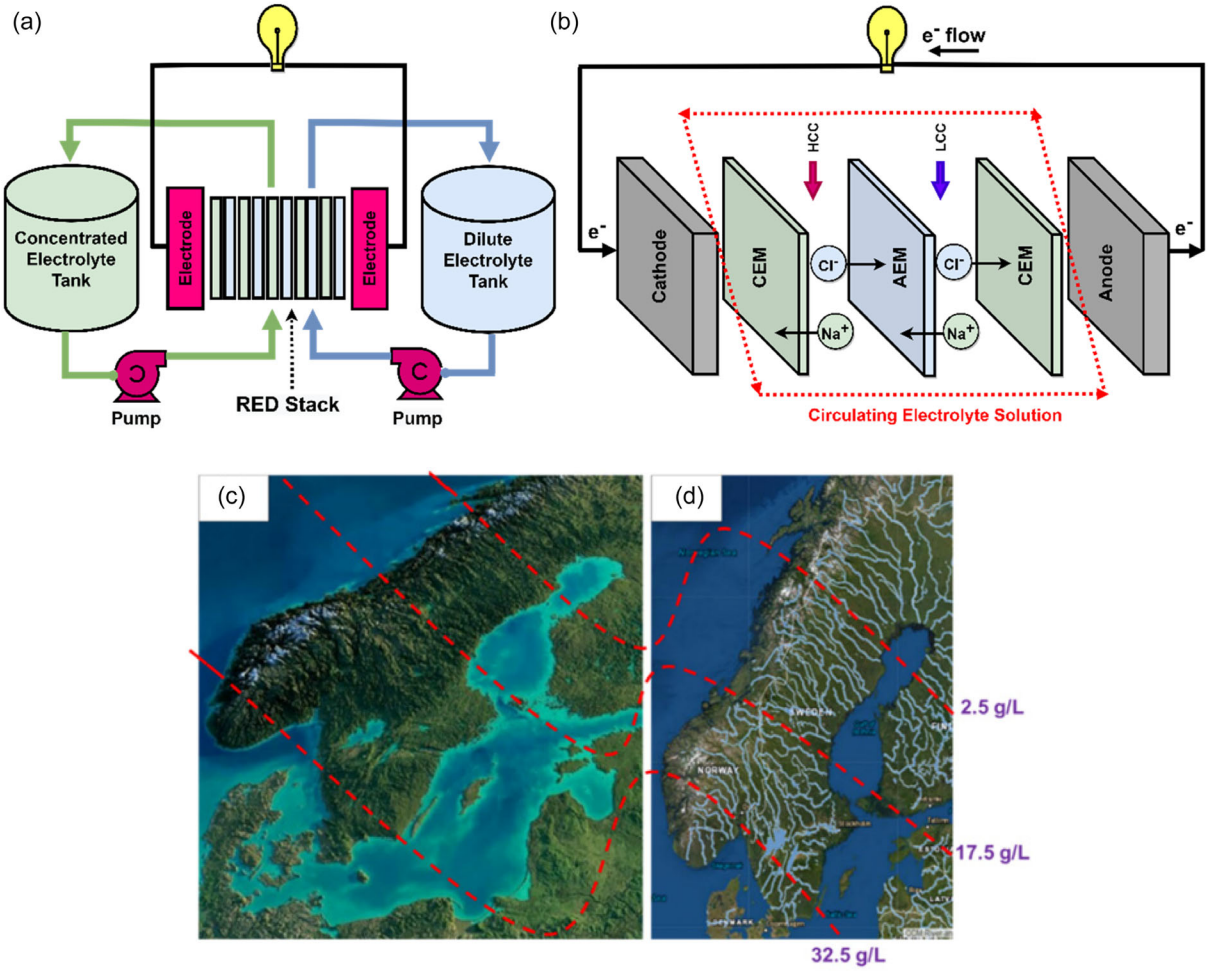

Figure 1. RED installation. a) A general schema, Adapted with permission.[57] Copyright 2018, Elsevier. b) A schema of one RED stack pair cell, Adapted with permission.[57] Copyright 2018, Elsevier. c) Coastal areas and d) various rivers to be used for SGP in Sweden, categorized into three geographical areas of low, intermediate, and high salinity.

Table 3. Factors and their considered levels for flow, salinity, and temperature.

Factor	Minimum level	Medium level	Maximum level
Sea Flow velocity [L h^{-1}]	5	15	25
River Flow velocity [L h^{-1}]	5	15	25
Sea Salinity [g L^{-1}]	2.5	17.5	32.5
Temperature [°C]	4.5	14	23.5

$$\begin{cases} V = RI \\ P = VI \text{ or } V^2/R \text{ or } RI^2 \end{cases} \quad (3)$$

The stack resistance (R_{stack}) and open circuit voltage (OCV) values can be obtained by the linear equation of the polarization (V–I) curves as shown in Equation (4).[33,34]

$$V = R_{stack} I + OCV \quad (4)$$

The slope of this line yields the R_{stack}, whereas the V-intercept indicates the OCV. The relationship between PD and current density (I_d) forms a first-order polynomial as described in Equation (5). Consequently, the I_d corresponding to the maximum PD ($PD_{,\,max}$) is determined as $I_d(P_{d,max}) = \frac{-b}{2a}$, which is then substituted into Equation (5) to obtain $PD_{,\,max}$. For simplicity, henceforth, this is denoted simply as PD.

$$PD = aI_d{}^2 + bI_d + c \quad (5)$$

2.3. ML

While uncovering typical patterns within a set of measurement and experimental data using unsupervised methods holds significance,[35–37] the authors of this study, drawing upon their prior knowledge of the experimental data, find supervised ML methods to be more effective.[38] The chosen ML predictor methods have been selected based on their good performance and are briefly explained as follows. The experimental dataset was

organized according to Equation (6). Here, the input samples are denoted as $x_i = [x_{i1}, x_{i2}, \ldots, x_{in}], i = 1, \ldots, m$, and the input features are represented as $f_j = [x_{1j}, x_{2j}, \ldots, x_{mj}]^T, j = 1, \ldots, n$. The m rows or n columns build the input matrix as $X_{m\times n} = [x_1, x_2, \ldots, x_m]^T$ or $X_{m\times n} = [f_1, f_2, .., f_n]$. The target or output is indicated by $Y_{m\times 1} = [y_1, y_2, \ldots, y_m]^T$. In our case, m equals 81 and n equals four. The input features consist of sea flow velocity (f_1), river flow velocity (f_2), sea salinity (f_3), and temperature (f_4). Y contains the PD values. The objective is to predict the vector of PD values Y donated by $\hat{Y}$, using input variables (in our case f_1, f_2, f_3, f_4) referred to here as predictors or features

$$X = \begin{bmatrix} Samp.\Downarrow/Feat. \Rightarrow & f_1 & f_2 & \ldots & f_n \\ x_1 & x_{11} & x_{12} & \ldots & x_{1n} \\ x_2 & x_{21} & x_{22} & \ldots & x_{2n} \\ \vdots & \vdots & \vdots & \vdots & \vdots \\ x_m & x_{m1} & x_{m2} & \ldots & x_{mn} \end{bmatrix}, Y = \begin{bmatrix} y_1 \\ y_2 \\ \vdots \\ y_m \end{bmatrix} \quad (6)$$

2.3.1. ML Predictor Methods

Ensemble Learning (EL)with Decision Trees (DT): EL enhances prediction accuracy by combining multiple models, especially for weak learners, such as a single DT.[39] Methods such as Bootstrap Aggregation (bagging), for example, Random Forest,[40] and Least Squares Boosting (LSBoost)[41] can be employed in EL regressor methods to aggregate the weak DT learners. LSBoost, utilized further in this paper, is a regression variation of boosting originally presented in the Adaptive Boosting method,[42] aiming at classification goals. EL with DT learners using LSBoost results in a robust predictive model by aggregating the predictions of individual trees. DTs partition the feature space into smaller regions and provide predictions based on the weighted averages of individual tree outputs, as indicated in Equation (7):

$$\hat{y}_i = \sum_{c=1}^{N} \alpha_c . DT_c(x_i) \quad (7)$$

Here, $\hat{y}_i$represents the predicted output, N is the total number of DTs used in EL, α_c is the weight assigned to the prediction of cth DT, and DT_c corresponds to the prediction of cth DT on the input normalized sample x_i.

Gaussian Process Regression (GPR): GPR represents a Bayesian nonparametric methodology for regression. This approach models the association between input features and output variable(s) as a distribution across functions, referred to as a Gaussian process, rather than discrete parameters. GPR offers a probabilistic framework for prediction using a kernel (covariance) function as indicated in Equation (8), which encapsulates uncertainty in predictions and enables robust estimation of model parameters.[43]

$$\hat{y}_i = k(x_i, \acute{x}_i)(K + \sigma^2 I)^{-1} y_i \quad (8)$$

In this context, y_i denotes the actual output for ith input sample, $k(.,.)$ represents a kernel (covariance) function, K stands for a covariance matrix of basic functions, σ is the initial value for the noise standard deviation and x_i and $\acute{x}_i$ denote input normalized samples in the training and testing sets, respectively.

ANN: ANNs are inspired by the structure and function of biological neural networks. ANNs are composed of interconnected nodes, arranged in layers that include input, hidden, and output layers. Through the iterative process of forward and backward propagation, ANNs acquire the ability to approximate complex nonlinear relationships between input variables and output(s) and generate predictions. When an ANN has between 1 to 3 hidden layers, it is categorized as a shallow neural network. However, as the number of hidden layers increases, the network transforms into what is known as a deep neural network. The relation between inputs and outputs in an L-hidden-layer ($L = 2$, in our case) ANN can be expressed as indicated in Equation (9) and (10):[44]

$$N^{(l)} = h(W^{(l)}. N^{(l-1)} + b^{(l)}), l = 1, 2, \ldots, L \quad (9)$$

$$\hat{Y} = f(W^{(L)}. N^{(L)} + b^{(L+1)}) \quad (10)$$

$N^{(0)} = [f_1, f_2, f_3, f_4]$ represents the input normalized vectors with four features specified as the input layer, $N^{(l)}$ represents the outputs from lth hidden layer, $W^{(l)}$ stands for weight matrices between neurons within (l-1)th and lth layers. $b^{(l)}$ shows bias vectors for the lth hidden layer. 'h' represents the activation function applied to the output of each hidden layer (sigmoid,[45] in our case), and f denotes the output activation function, such as linear in regression tasks. In our case, it was defined as "none", indicating that the network can directly output the continuous values without further transformation. Finally, the output prediction vector is denoted as $\hat{Y}$.

2.3.2. Cross Validation and Evaluation

Given the moderate size of our dataset, ensuring a reliable evaluation of the ML methods was crucial. Therefore, a fivefold cross-validation technique[46] was employed on the ML models. This technique involved randomly partitioning the dataset into five equal subsets (in our case, $81/5 \approx 16$). The models were trained on four subsets and tested on the remaining one, with this process repeated five times to ensure that the entire dataset was eventually used for testing. By employing this technique, we also mitigated the risk of overfitting the methods to specific parts of the dataset.

The evaluation criteria utilized in this study consist of two common metrics employed in regression tasks:[47] Root mean squared error (RMSE) and R-squared (R^2), as depicted in Equation (11) and (12), where *"Corr"* represents the Pearson correlation coefficient (PCC).

$$RMSE = \sqrt{\frac{1}{m}\sum_{i=1}^{m} (y_i - \hat{y}_i)^2} \quad (11)$$

$$R^2 = Corr.(Y, \hat{Y})^2 = 1 - \frac{\sum_{i=1}^{m} (y_i - \hat{y}_i)^2}{\sum_{i=1}^{m} (y_i - \overline{y_i})^2} \quad (12)$$

2.3.3. Feature Importance

Besides applying ML predictor methods to identify the most significant predictor (feature) among the four input variables for predicting *PD*, two statistical methods,[48] correlation analysis and F-test algorithm, were utilized to assess feature importance. These methods were used to calculate the PCCs and the negative logarithm of the p-values ($-\log(p)$) between each input feature f_1, f_2, f_3, f_4 individually, and the *PDY*, respectively. The p-value represents the statistical measure used to assess the validity of a hypothesis against observed data. Higher scores obtained from both methods indicate the greater significance of the respective input feature.

2.4. LCA

This LCA study aims to evaluate the potential environmental impacts of the RED system, with the objective of guiding its development from a sustainability perspective. In this analysis, the functional unit was defined as the lifetime energy generated by the RED plant, measured in megawatt-hours (MWh), having a lifetime of 25 years. This unit represents the total amount of net electricity delivered to the grid. The plant sizing was determined by estimating the net power available in the system, based on the flow of available water, and then calculated the required membrane area to generate this power. Net power production, as stated in Equation (13), was derived from the available water quantities, the theoretical energy density (ED) of the feedwater streams, and the plant's efficiency, as outlined in the methodology stated in.[28]

$$P_{\text{net}} = Q \times ED_{\text{water}} \times \eta_{\text{plant}} \tag{13}$$

Where P_{net} represents the net power production in (MW), Q is the water flow rate of the plant in ($m^3\ s^{-1}$), ED_{water} denotes the theoretical ED of the water in ($MJ\ m^{-3}$), and η_{plant} is the conversion efficiency of the plant.

As illustrated in Equation (14), the membrane area required for the plant's lifespan was determined by the plant's power production, the membrane *PD*, and the membrane and plant lifetimes.

$$A_{\text{membrane}} = \frac{(P_{\text{net}}/\eta_{\text{plant}})}{PD_{\text{membrane}} \times \left(\frac{L_{\text{plant}}}{L_{\text{membrane}}}\right)} \tag{14}$$

Where A_{membrane} (m^2) represents the membrane area required over the lifetime of the plant, PD_{membrane} denotes the *PD* normalized to the membrane surface area, L_{plant} is the Plant's lifetime, and L_{membrane} refers to the membrane's lifetime.

The system boundary under evaluation included the environmental impacts that result from natural resources utilization, water pretreatment facility, component manufacturing, operational activities, as well as end-of-life practice (**Figure 2**). The assembly of the RED stack system comprises the materials and processes required for constructing a membrane stack, incorporating cathode and anode membrane material, Polypropylene (PP) endplates, spacer gaskets, electrodes (Ti mesh coated with Ru-lr), Polyvinyl Chloride (PVC), and PP water pipes and containers. However, the construction of the site was not included in this analysis.

2.4.1. Life Cycle Inventory (LCI)

LCI analysis phase entails the compilation of an inventory of input and output data that was relevant to the system being investigated. In this analysis, inventory data were gathered from both lab-scale primary data and peer-reviewed articles.[31,49] The water requirements for Seawater-River RED systems fluctuated based on the accessibility of water sources and the intended power

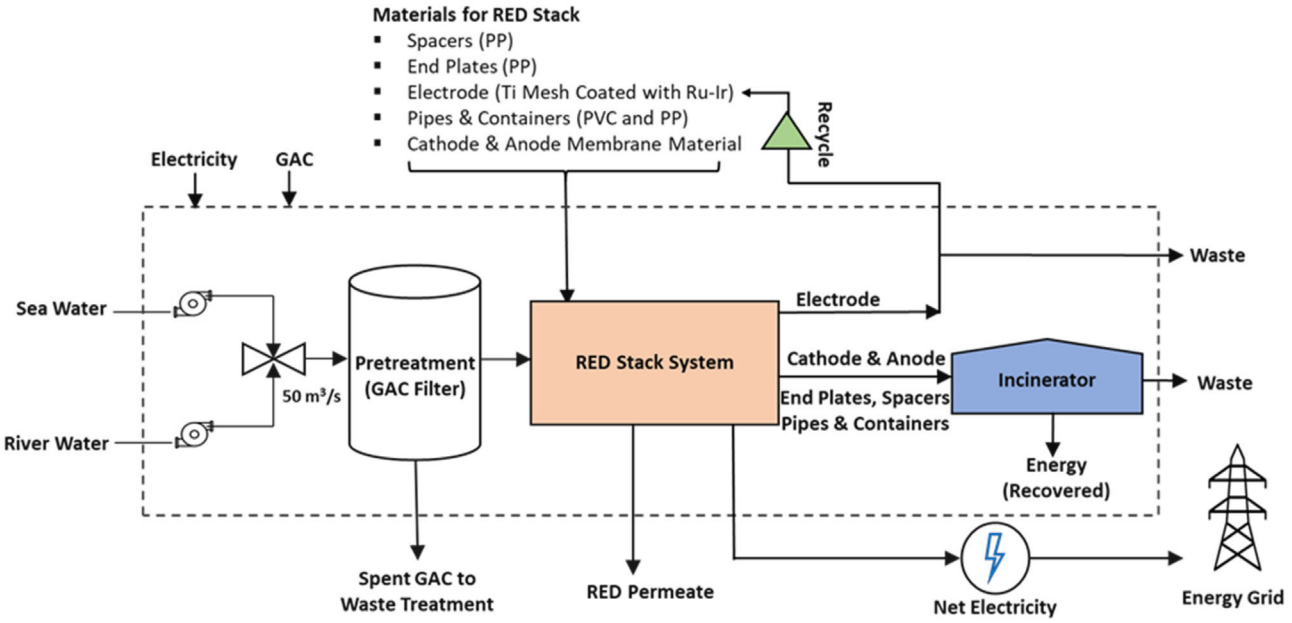

Figure 2. System boundary diagram for energy generation by the Seawater-River RED system.

generated by the facility. For this assessment, 35 and 15 $m^3 s^{-1}$ of concentrated and diluted water were used, respectively, and water was conveyed from the source to the plant through pumping. In the seawater-river analysis, granular activated carbon (GAC) was considered for water pretreatment (0.1 kg per cubic meter of water).[49] The estimated lifetime of the GAC filter ranges between 8 and 10 years, with an 8-year lifespan assumed for this study (**Table 4**). Over the 25-year operational lifetime of the salinity gradient plant, it is anticipated that the GAC filters will need to be replaced three times. Consequently, the total GAC required for the entire lifespan of the plant was estimated to be 1,296 tons. However, the spent GAC produced during the water pretreatment process was categorized as waste and was not considered within the scope of this analysis.

During plant operation, RED facilities generated their own electricity, with about 25% of gross power consumed internally for operations, mainly pumping. The net electricity production reflects this difference.[50] Therefore, the facility's net efficacy was estimated to be 75%. The net power production for this Seawater-River RED system was assumed as 60 MW. The Swedish electricity grid was used for modeling electricity for the operation of both RED systems. Due to the extensive membrane area required throughout the lifespan of a RED facility, the environmental impacts associated with membrane production constitute a substantial component of the LCI. According to published estimates, the lifespan of membranes typically falls between 5 to 7 years.[51] This reduction in lifespan was observed due to the ageing and fouling of the membranes. For this analysis, a membrane lifetime of 6 years was selected. Waste incineration at a municipal facility was employed to simulate the end-of-life stage of the PP and PVC products, which were classified as plastic waste from the RED stack. However, the Ti electrode was assumed to be recycled. The brine-wastewater treatment plant (WWTP) scenario utilized a combination of brine and WWTP for electricity generation, with the potential to be implemented as a modular, portable system. This approach leverages the energy from concentrated brine, a byproduct of desalination, sea salt production, and industrial processes. Here, the brine flow rate limits electricity production, while WWTP water was assumed unlimited. **Table 5** summarizes the brine-WWTP RED system properties.

Table 4. Seawater-River RED system property summary.[31,49]

Lifecycle Stage	Parameter	Description and Assumptions
Water Pumping	Flowrate	Total flowrate: 50 $m^3 s^{-1}$ (Seawater: 35 $m^3 s^{-1}$, River Water: 15 $m^3 s^{-1}$); Daily Plant flowrate: 4 320 000 $m^3 d^{-1}$
Pretreatment (GAC Filtration)	Amount Needed per Lifetime	GAC required: kg m^{-3}; GAC lifetime: 8 years; Total GAC required: 1 296 tons
RED Stack System Installation	Materials Used for Membrane Construction & plant lifetime	Membrane lifespan: 6 years; Plant lifetime: 25 years; PD = 3.5 W m^{-2}; ED = 1.6 MJ m^{-3}
Membrane	Area	Total membrane area: 5 494 506 m^2
RED Stack System Operation	Lifetime Energy Generation	Lifetime energy generation: 12 600 000 MWh; Net power production: 60 MW (based on 8400 h $year^{-1}$ over 6 years with 4 membrane changes in 25 years)
Red Stack System Decommissioning	–	Plastic parts (spacers, end plates, pipes, containers) sent to incineration with energy recovery credit; Metal parts (Ti-coated electrodes) recycled with credit for Ti recovery.

2.4.2. Life Cycle Impact Assessment

To assess the impacts associated with RED technology, the ReCiPe World (H) midpoint impact assessment methodology was employed in this study.[52] **Table 6** lists the selected midpoint impact categories for this analysis and their corresponding impact indicators.

2.4.3. Interpretation and Scenario Analysis

In this LCA study, a scenario analysis was performed by investigating a variety of configurations involving various electrode materials, including Titanium electrodes (as baseline scenario), polyacrylonitrile carbon fiber (PAN-CF), and lignin-CF electrodes. PAN-CF electrodes are carbon fiber electrodes made from polyacrylonitrile, offering high electrical conductivity, mechanical strength, and chemical stability for use in electrochemical applications.[53] In contrast, Lignin-CF electrodes are derived from lignin, providing a sustainable alternative with good electrical conductivity and mechanical properties for use in electrochemical applications.[54] The scenarios were designed to evaluate how variations in electrode types influence the system's

Table 5. Brine-WWTP RED system property summary.

Lifecycle stage	Parameter	Description and assumptions
Water pumping	Flowrate	Total flowrate = 0.05 $m^3 s^{-1}$; Daily Plant flowrate = 4320 $m^3 d^{-1}$
Pretreatment (GAC Filtration)	Amount needed per lifetime	GAC required: kg m^{-3}; GAC lifetime: 10 years; Total GAC required: 864 kg
RED stack system installation	Materials used for membrane construction & plant lifetime	Membrane lifespan: 6 years; Plant lifetime: 25 years; PD = 6 W m^{-2}; ED = 15 MJ m^{-3}
Membrane	Area	Membrane area total= 30 049 m^2
RED stack system operation	Lifetime energy generation	Lifetime energy generation: 118 125 MWh; Net power production: 0.5625 MW (based on 8400 h $year^{-1}$ over 6 years with 4 membrane changes in 25 years)
RED stack system decommissioning	–	Plastic parts (spacers, end plates, pipes, containers) sent to incineration with energy recovery credit; Metal parts (Ti-coated electrodes) recycled with credit for Ti recovery.

Table 6. Summary of the midpoint impact categories and impact indicators.

Impact Category	Indicator	CFm	Abbrev	Unit
Climate Change	Infrared radiative forcing increases	Global warming potential	GWP	kg CO2 eq
Ozone Depletion	Stratospheric ozone decrease	Ozone depletion potential	ODP	kg CFC-11 eq
Ozone formation, Human Health	Tropospheric ozone increase	Photochemical oxidant formation potential: ecosystems	POFP	kg NOx eq
Fine; Particulate matter; formation	$PM_{2.5}$ population intake increases	Particulate matter formation potential	PMFP	kg PM2.5 eq
Terrestrial acidification	Proton increase in natural soils	Terrestrial acidification potential	AP	kg SO2 eq
Freshwater eutrophication	Phosphorus increase in freshwater	Freshwater eutrophication potential	FEP	kg P eq
Freshwater ecotoxicity	Hazard-weighted increase in fresh waters	Freshwater ecotoxicity potential	FETP	kg 1,4-DCB eq
Human toxicity: cancer	Risk increases of cancer disease incidence	Human toxicity potential	HH-CP	kg 1,4-DCB eq
Human toxicity: non-cancer	Risk increase of noncancer disease incidence	Human toxicity potential	HH-NCP	kg 1,4-DCB eq
Fossil resource scarcity	upper heating value	Fossil fuel depletion potential	FDP	kg oil eq

overall environmental performance, providing a thorough analysis of potential enhancements and trade-offs in RED technology.

3. Results and Discussions

3.1. SGE and ML Interpretation Besides the Results

The polarization intensity curve (V vs. I) and the resulting PD variation as a function of current density for experiments performed at different temperatures (i.e., 21, 15, and 8 °C, respectively) and using different salinity gradients (i.e., 2.5, 17.5, and 32.5 g L^{-1}, respectively), are shown in **Figure 3**. In the polarization intensity curves, there is a significant decrease in the slope as the HC concentration increases, resulting in a reduction in the stack resistance.

This is due to the increase in electrical conductivity, which decreases resistance. There is also a decrease in the slope of curves as the temperature increases. This might be due to an increase in ion mobility and, thus, an increase in the electrical conductivity of the solutions. In contrast, an increase in the concentration of HC increased OCV. This is because OCV is defined where there is no current flowing through the system. In this case, OCV is primarily a function of HC concentration. As the HC concentration increases, the chemical potential will also increase, resulting in increased OCV. Figure S1–S4 (Supporting Information) illustrate the impact of adjusting operating parameters—sea flow velocity, river flow velocity, sea salinity, and temperature—on PD, stack resistance, and open-circuit voltage (**Figure 4**).

Given that the ML methods are strongly dependent on the selection of their hyperparameters, we carried out a

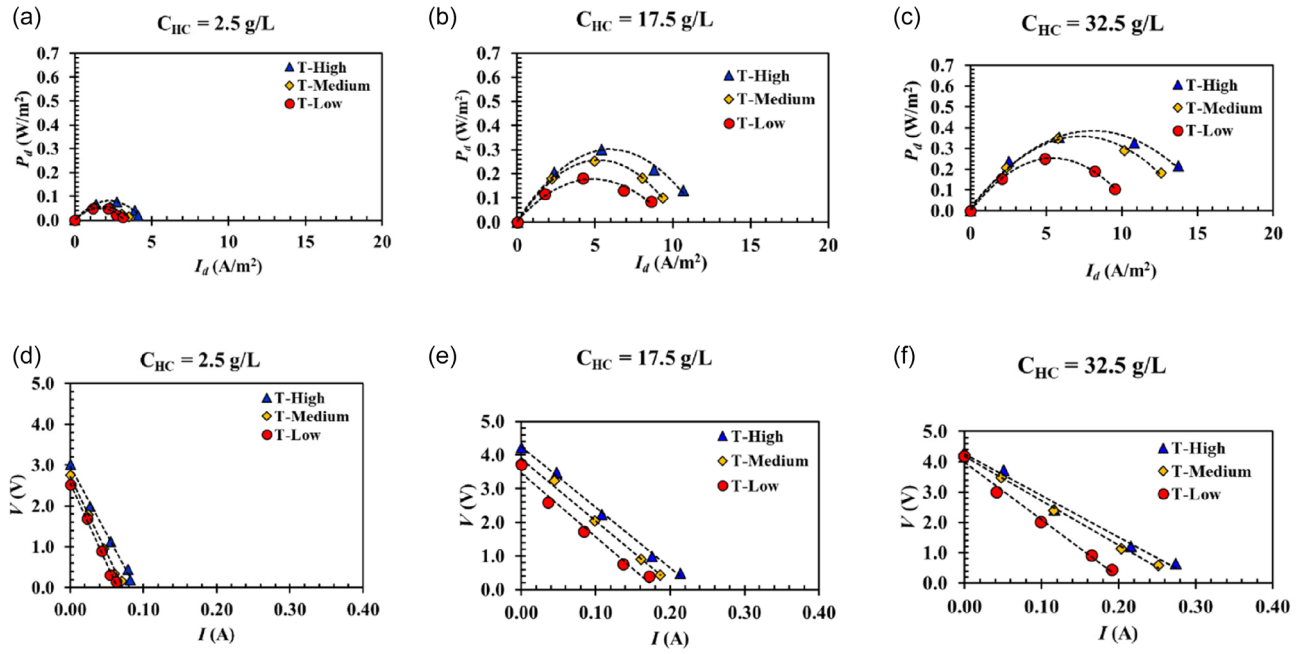

Figure 3. a–c) RED stack response regarding PD versus current density and d–f) polarization intensity curves for varying concentrations and temperatures at a constant flux of 10 L h^{-1}.

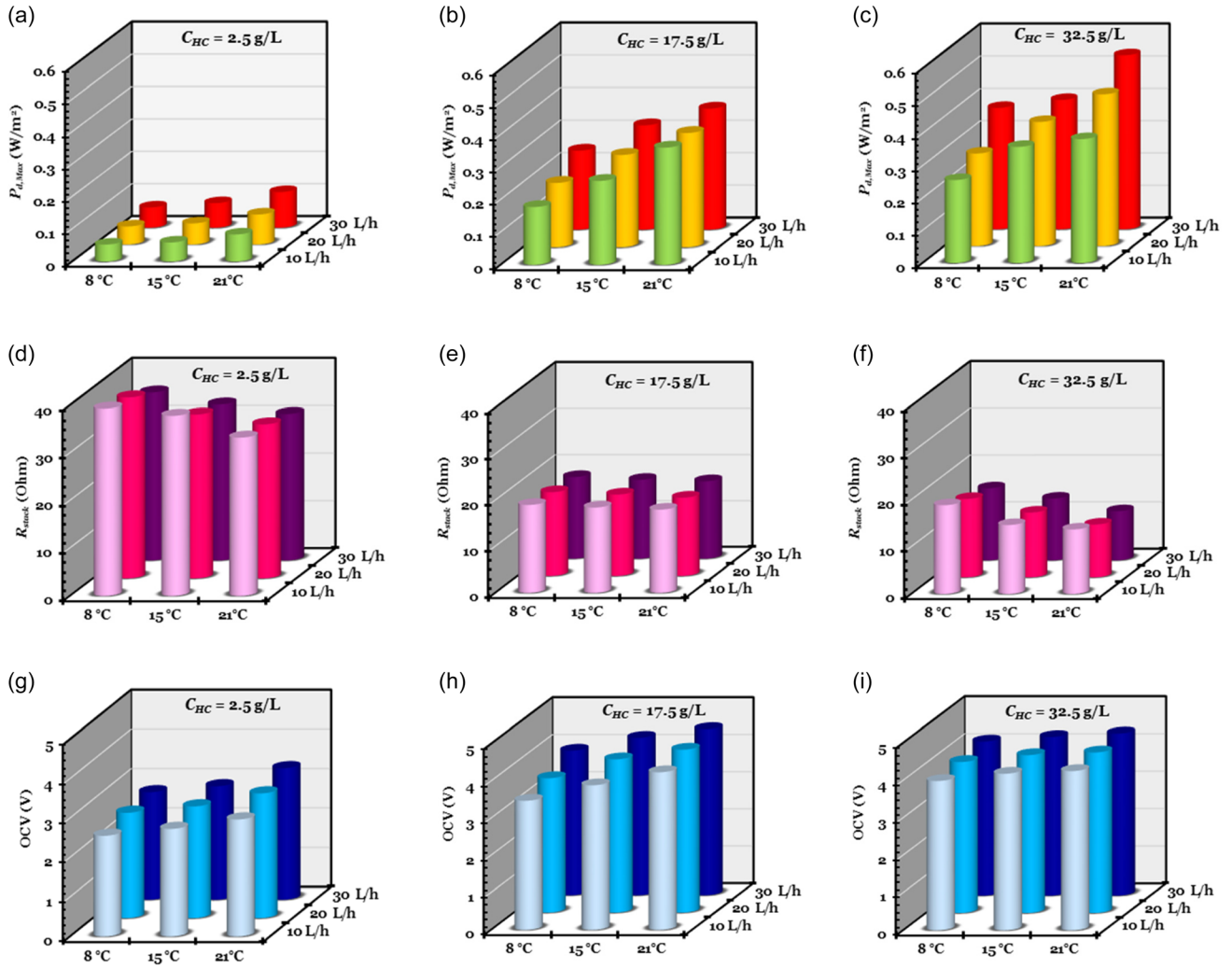

Figure 4. a–c) Experimental result of the RED system in terms of *PD*; d–f) stack resistance; and g–i) open-circuit voltage operating with 2.5, 17.5, and 32.5 g L^{-1} of SSW solutions, respectively.

hyperparameter optimization using Bayesian optimization during the training of the ML methods, and the results are given in **Table 7**. The comparison between predicted and experimental *PD* values, both collectively (one V.S. one) and individually plotted against record numbers from those 81 experiments, is presented in **Figure 5**. Predictions are produced utilizing three optimized ML methods: an ensemble method with DT weak learners, the GPR method, and a custom-designed ANN. Furthermore, the performance of each method is assessed using fivefold cross validation based on RMSE and R^2, which are displayed on top of subplots in Figure 5a–c. The RMSE and R^2 values for each method are as follows: for the Ensemble method, the values are 2.448 and 98.7049; for GRP, they are 1.9574 and 99.1757, and for ANN, they are 1.7372 and 99.3495. Notably, the results highlight the superior predictive capability of the ANN method, evidenced by its lowest RMSE and highest R^2, followed by the GRP method, thus indicating their efficiency in *PD* prediction compared to the Ensemble approach.

While GPR and ANN performed well on our experimental dataset, it's important to note that GPR can be computationally expensive in real applications, and ANN can be complex, though it performs reliably with smaller datasets.[55] This study used fivefold cross validation to confirm the reliable performance of ANNs, even with limited data, among ML methods.

The 3D surfaces in **Figure 6** present the impact of the changing operating parameters on *PD*. The filled dot points represent the experimental data points, while the hollow dot points depict predictions generated by the best ML-based predictor, the ANN. Considering all aspects of Figure 6a–c, irrespective of seasonal temperatures, higher sea salinity values correlate with increased *PD* extraction. In Figure 6a–c, which include three seasonal temperature levels, a rise in temperature also positively affects *PD*. Both sea flow velocity and river flow velocity demonstrate a positive correlation with *PD*, as depicted in Figure 6a–c. However, at higher temperatures, particularly during summer at 23.5 °C, and higher sea salinity i.e., 32.5 g L^{-1}, sea flow velocity shows a notably strongr positive impact on *PD* than river flow velocity. In

Table 7. Optimal hyperparameter values for the ML methods.

ML method	Hyperparameter	Range	Optimal value
Ensemble-DT	Method	Bag, LS-Boost	LS-Boost
	Num Learning Cycles/Num Trained	[10,500]	420
	Learn Rate	[1×10^{-3}, 1]	0.1855
	Min Leaf Size	[1,40]	2
	Max Num Splits	[1,80]	7
	Num Variables to Sample	[1,4]	4
GPR	σ	[1×10^{-3}, 2.1645]	3.18×10^{-4}
	Basic Function	Constant, none, linear, pure Quadratic	none
	Kernel Function	Ard exponential, ardmatern32, ardmatern52, hard rational quadratic, exponential, rational quadratic, squared exponential, etc	ardmatern32
	Kernel Scale	[0.0024, 2.4343]	NaN
ANN	Num Layers	[1,5]	2
	Activations	Relu, tanh, sigmoid, none	"sigmoid" for hidden layers and "none" for output layer
	Lambda	[1.23×10^{-07}, $1.23 \times 10^{+03}$]	3.37×10^{-06}
	Layers Size	[1,400]	[302, 41]

Figure 6c, the highest extracted *PD* recorded was 1.1605 w m^{-2}, predicted by the ANN as 1.1737 w m^{-2}, with the highest temperature, 23.5 °C, and the highest sea and river flow velocities at 25 L H^{-1}.

As observed in Figure 6d–f, irrespective of river flow velocity levels, increasing sea salinity values have a positive impact on *PD* extraction, as demonstrated in Figure 6a–c as well. This is due to the increase in salinity, which causes *OCV* and *V* to increase, while the number of free ions in the concentrated solution rises. This increase boosts conductivity, decreases R_{stack}, and results in higher *PD*. From Figure 6d–f, representing three river flow velocity values, a rise in flow shows only a very shallow positive effect on *PD* because it flushes ions from the dilute side, maintaining a low concentration on that side. However, this effect remains very small. Increasing temperature and sea flow velocity together lead to a higher *PD*, with this finding being much clearer for higher sea salinity values. The free ions in the solutions become more active as temperature rises, increasing ion migration and enhancing the potential difference on both sides of the ion exchange membranes (IEMs), which increases *OCV*. The conductivity of the solution is also improved with an increase in temperature, reducing *R*stack and boosting *PD* extraction. Across Figure 6g–i, depicting three sea flow velocity values, a rise in flow from 5 to 15 L h^{-1} shows only a very slight positive impact on *PD*. In contrast, raising the flow to 25 L h^{-1} exhibits a more pronounced positive effect (due to a high salinity gradient). From Figure 6a–c, it is evident that the impact of sea salinity is more significant than that of temperature. This distinction becomes even clearer at higher sea flow velocity values, as shown in Figure 6i.

The results of applying the feature importance extraction methods are depicted in **Figure 7**. Both methodologies yield consistent importance rankings: sea salinity (f_3) is the most significant, followed by temperature (f_4), (that was observed from Figure 7a–c too), sea flow velocity (f_1), and river flow velocity (f_2), with sea salinity exerting a notably pronounced impact compared to the other variables.

3.2. LCA Results

3.2.1. System 1: Seawater-River RED System Impact Analysis

The LCA of the seawater-river RED system reveals a diverse range of environmental impacts across various categories, with notable contributions to global warming, human health, and resource depletion. In the climate change category, the system results in a global warming potential (GWP) of 178 g CO_2 eq. per kWh of energy produced, based on the total energy output of 12.6 million MWh over its life cycle of the RED system. This is attributed to the energy-intensive processes involved in Ti electrode production and operational energy use for pumping. Although stratospheric ozone depletion is on a lower scale at 1416 kg chlorofluorocarbon equivalent (CFC11eq), this impact is because of the ozone-depleting substances in the manufacturing of electrodes (56%) and the pumping process (40%). In terms of impacts from ozone formation and fine particulate matter formation, Ti electrodes contribute 82–86% of the impact, whereas pumping contributes for the remaining 12–18%. A similar trend was seen for the terrestrial acidification category, further demonstrating the significant release of sulfur oxides from industrial processes associated with electrode production and fuel combustion.

Freshwater eutrophication highlights the impact of nutrient runoff and toxic chemical discharges into aquatic systems, where contribution analysis indicated most impacts (76%) come from Ti electrode production. Pumping, in contrast, accounts for ≈71% of the impact in the freshwater ecotoxicity. The system also shows substantial human toxicity impacts, with carcinogenic and non-carcinogenic toxicities amounting to 1.66×10^9 kg 1,4-Dichlorobenzene (1,4-DCB) and 6.8×10^9 kg 1,4-DCB, respectively. These findings emphasize the presence of harmful substances throughout the RED life cycle, particularly in the production and handling of membranes and other components. Lastly, the fossil resource scarcity impact is 4.97×10^8 kg oil eq, reflecting the system's reliance on fossil fuels for its energy inputs, particularly during electrode production (87%). **Figure 8**a presents the contribution analysis for the seawater-river RED system, highlighting that the production of Ti electrodes and the energy required for pumping account for the majority of environmental impacts across all assessed categories.

3.2.2. System 2: Brine-WWTP System Impact Analysis

The results for the brine-WWTP RED system reveal a similar trend, with the majority of environmental impacts arising

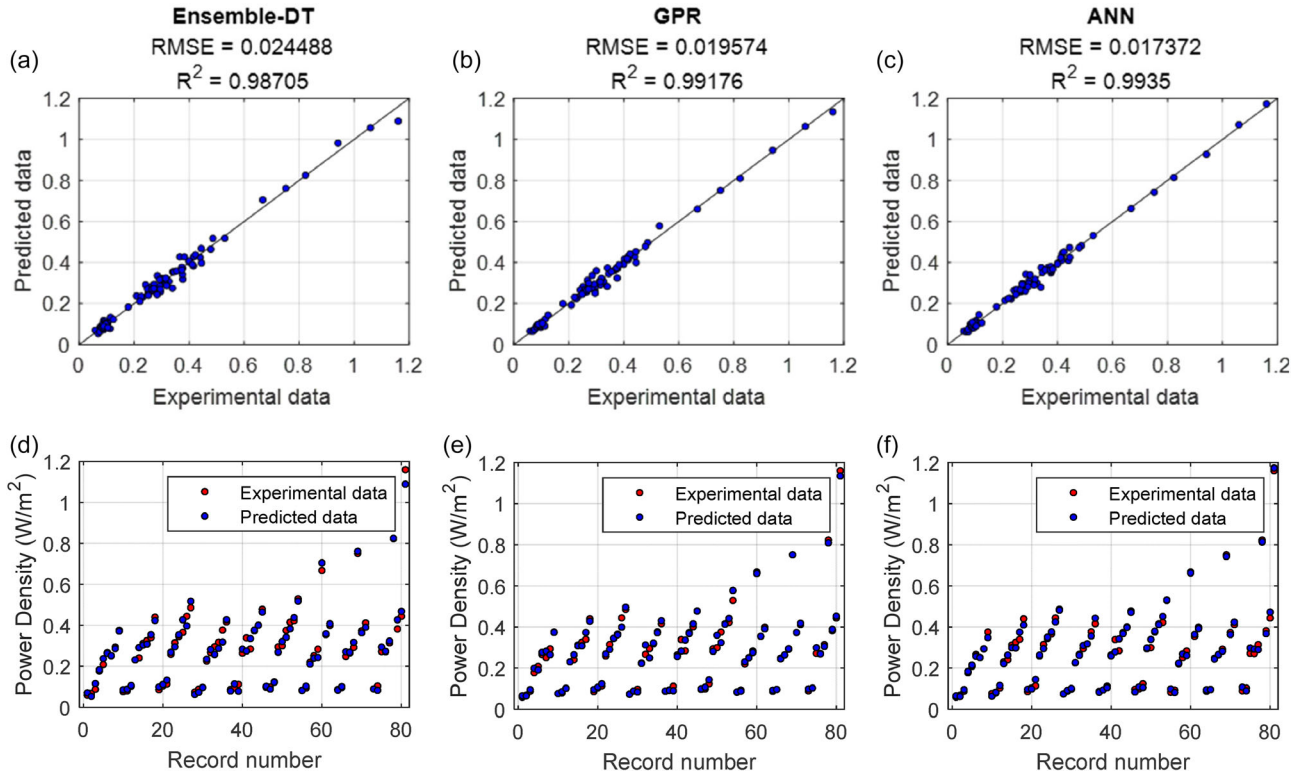

Figure 5. Comparison of predicted and experimental *PD*: a,d) Ensemble; b,e) GRP; c,f) ANN. Validation RMSE and R^2 values are shown at the top of each subfigure (a), (b), and (c).

primarily from Ti electrode production and pumping activities (Figure 8b). The system contributes 158 g CO_2 eq/kWh of energy produced, based on a total energy output of 118 125 MWh. This carbon footprint is driven by the manufacturing processes for key components, such as electrodes, and operational energy demands for pumping, as discussed before. The system's stratospheric ozone depletion potential of the system is 49 kg CFC11 eq, whereas it also shows considerable impacts on ozone formation related to human health, with 53416.97 kg Nitrogen oxides (NO_x) eq. This result implies that nitrogen oxide emissions which contribute to ground-level ozone and degrade air quality. Furthermore, the system produces 39119.09 kg Particulate matter with a diameter of 2.5 micrometers ($PM_{2.5}$) eq of fine particulate matter, highlighting the potential harm from airborne particles, mainly produced during the electrode production (81%). In terms of terrestrial acidification, the system contributes 106156.83 kg SO_2 eq, indicating substantial emissions of acidifying substances like SO_2. These emissions, largely generated from electrode production, can damage soil health and biodiversity.

The Brine-WWTP RED system also presents a high FEP of 43 336.58 kg P eq. In terms of toxicity impacts, the results for freshwater ecotoxicity (2.2×10^6 kg 1,4-DCB), human carcinogenic toxicity (6.89×10^8 kg 1,4-DCB), and human non-carcinogenic toxicity (1.0×10^8 kg 1,4-DCB) were found, where pumping and electro production are found mainly responsible for the impacts. Finally, the fossil resource scarcity result of 3 761 601.27 kg oil eq reveals the system's reliance on nonrenewable energy sources throughout its lifecycle.

3.2.3. Scenario Analysis: Seawater-River RED System

The comparative analysis of the environmental impacts from different electrode materials in the seawater-river RED system reveals significant variations across the impact categories (Figure 8c). The baseline materials (Ti electrode), show a significantly higher climate change impact when compared to both PAN CF and Lignin Carbon Fiber (Lignin CF) electrodes. The PAN CF electrode achieves a substantial reduction in GWP, resulting in ≈80.15 g CO_2 eq per kWh of energy produced, reflecting a 54% decrease from the baseline. Lignin CF electrodes offer even greater environmental benefits, reducing GWP to 33.73 g CO_2 eq/kWh, marking an 81% decrease compared to the baseline. These results indicate that both PAN CF and lignin CF electrodes are more sustainable alternatives, with lignin CF emerging as the most efficient choice for minimizing greenhouse gas emissions.

Stratospheric ozone depletion, a decrease in atmospheric total ozone due to ozone-depleting substances in any process system, shows a more complex trend in terms of electrode materials. The baseline Ti electrode shows a relatively lower impact, recording 1416 kg CFC11 eq. In contrast, the PAN CF electrode significantly increases this impact to 4691 kg CFC11 eq, a threefold rise. Lignin CF electrodes demonstrate a slightly better performance with an impact of 4293 kg CFC11 eq, making them a more favorable option than PAN CF. However, both carbon-based electrodes show higher ozone-depleting potential compared to baseline Ti electrodes. This trade-off is important to consider, especially in regions where ozone layer protection is a priority.

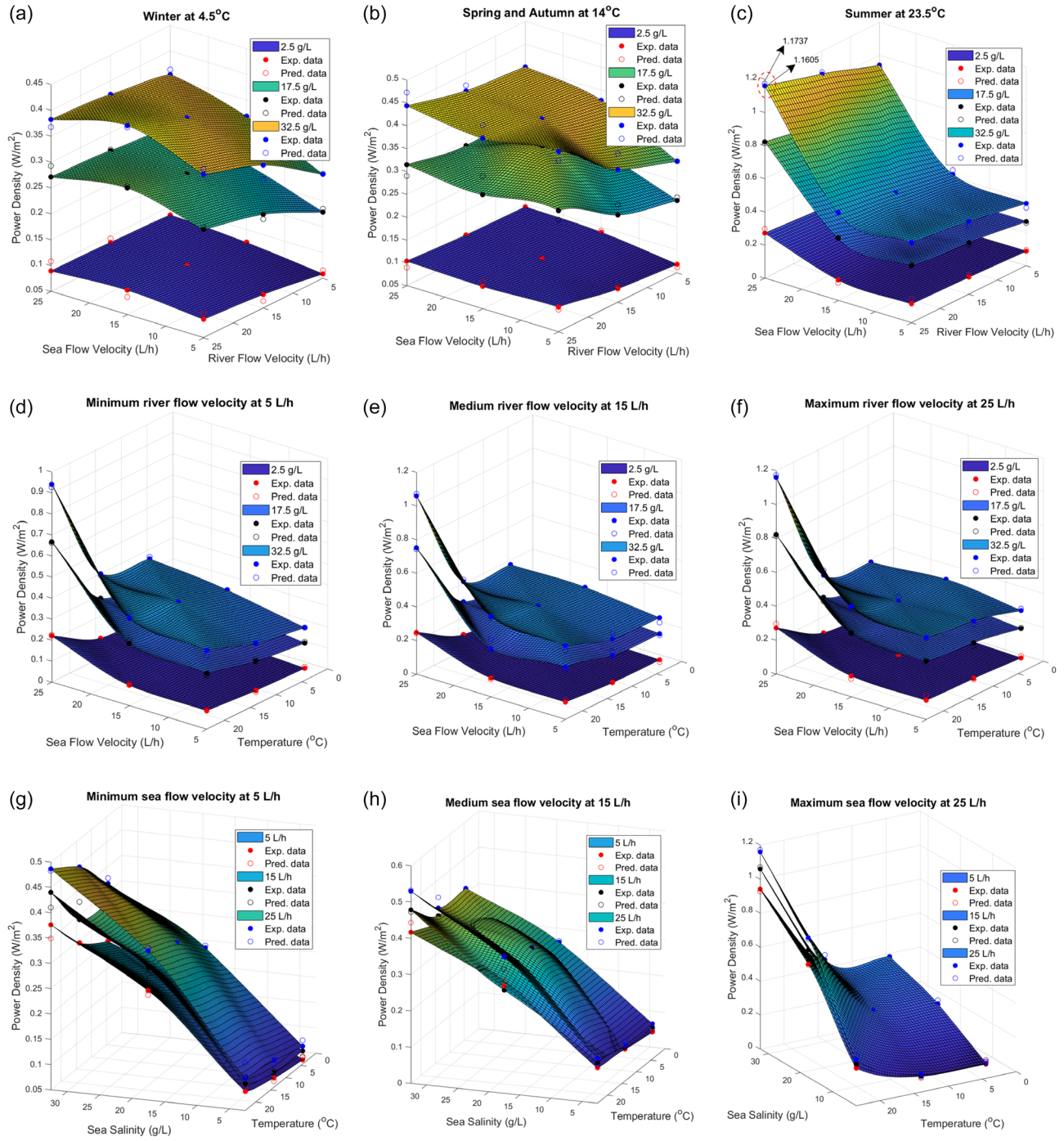

Figure 6. a–c) Impact of sea/river flow velocity on *PD* at three salinity levels; d–f) Impact of flow velocity and temperature on *PD* at three salinity levels; g–i) Impact of sea salinity/temperature on *PD* at three river flow levels. Filled dots are experimental data; hollow dots are predictions from ANN.

The substantial reduction in ozone formation and fine particulate matter further supports the environmental advantages of Lignin CF electrodes. Ozone formation impact is reduced from 7.44×10^6 kg NO_x eq in the baseline to 2.45×10^6 kg NO_x eq with PAN CF, and even further to 1.32×10^6 kg NO_x eq with lignin CF, showing a reduction of 64% and 82%, respectively. Similarly, fine particulate matter formation sees a substantial decline, with lignin CF reducing it to just 2.77×10^5 kg PM2.5 eq, a 96% decrease from the baseline. These results highlight the superior environmental performance of lignin CF in reducing air quality-related impacts.

In terms of, Both PAN CF and lignin CF significantly reduce terrestrial acidification impact compared to Ti electrodes. PAN CF shows a reduction to 7.61×10^6 kg SO_2 eq from the baseline

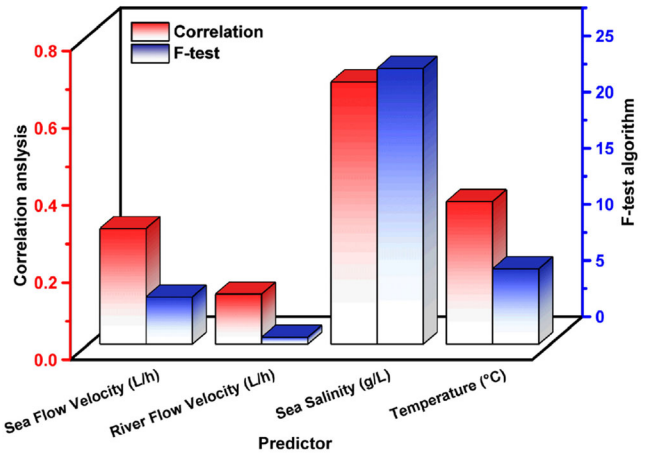

Figure 7. Predictor (feature) importance scores by correlation analysis and F-test algorithm.

1.81×10^7 kg SO_2 eq, and lignin CF achieves an even greater reduction to 1.32×10^6 kg SO_2 eq, nearly 93% less than the baseline. This indicates that lignin CF electrodes offer the best performance in mitigating acid rain and other acidification-related environmental concerns. However, freshwater eutrophication tells a different story. Both PAN CF and lignin CF electrodes exhibit much higher impacts compared to the baseline. PAN CF electrodes result in a fourfold increase in eutrophication potential, reaching 4.16×10^6 kg P eq, and lignin CF follows closely with 3.82×10^6 kg P eq. This suggests that while carbon fiber electrodes offer many environmental benefits, they may make worse issues related to nutrient loading and water quality, which should be addressed in future designs.

Freshwater ecotoxicity and human carcinogenic toxicity also see significant reductions with carbon-based electrodes. PAN CF reduces freshwater ecotoxicity by 86% compared to the baseline, while Lignin CF further improves this to an 87% reduction. Human carcinogenic toxicity, a critical health impact category, also drops by over 90% with both carbon fiber electrodes compared to Ti. Despite this, the human non-carcinogenic toxicity remains relatively high for both PAN CF and Lignin CF, even surpassing the baseline Ti electrode impacts. This suggests that while carbon-based electrodes improve health-related toxicities in certain areas, challenges remain in addressing non-carcinogenic toxicity concerns. Lastly, fossil resource scarcity is markedly lower for both PAN CF and Lignin CF electrodes compared to Ti. Lignin CF, in particular, performs best with a drastic reduction to just 7.11×10^6 kg oil eq, which is over 98% lower than the baseline, indicating that lignin CF is the most sustainable choice when considering resource use.

The scenario analysis of the brine-WWTP RED reveals that Lignin CF electrodes have lower impacts across all categories compared to the PAN CF and the baseline scenario

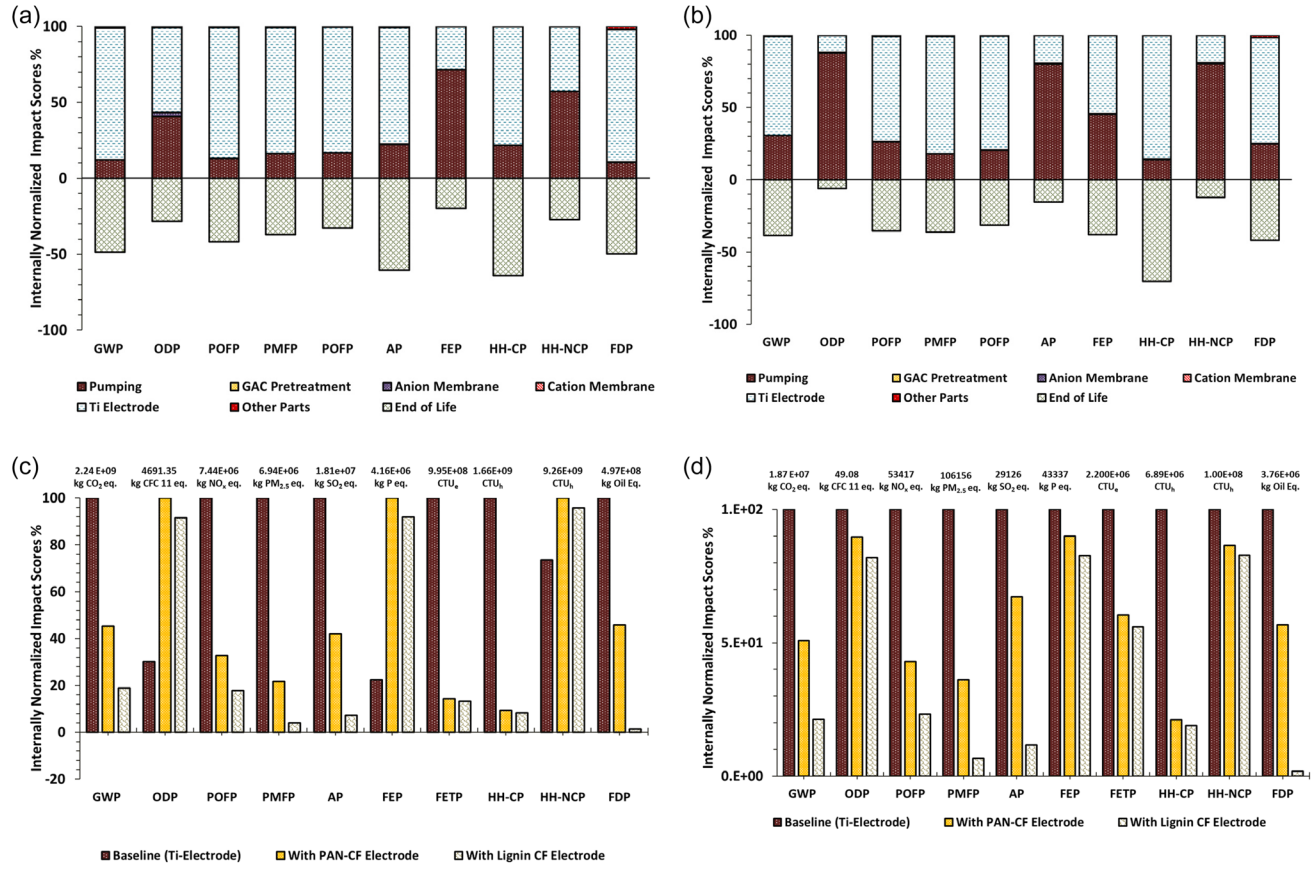

Figure 8. a,b) Contribution c,d) and scenario for (a,c) Seawater-River RED system; (b,d) Brine-WWTP RED system.

(Figure 8d). In terms of climate change impact, the PAN CF electrode results in ≈49% decrease in CO_2 emissions compared to the baseline, reducing emissions to 80 g CO_2 eq per kWh. The Lignin CF electrode further reduces emissions by about 79%, reaching 33.7 g CO_2 eq per kWh. This reflects a substantial improvement in reducing carbon emissions with alternative electrodes.

For stratospheric ozone depletion, the PAN CF electrode improves performance by 10%, while the Lignin CF electrode shows a slightly better improvement of around 18%, resulting in a final impact of 40.24 kg CFC-11 eq. Regarding ozone formation impacting human health, the PAN CF electrode reduces the impact by 57% compared to the baseline; however, Lignin CF performs even better with a 77% reduction. The reduction in fine particulate matter formation is especially pronounced with lignin CF, which achieves a 93% decrease compared to the baseline, lowering the impact from 39 119.10 kg PM2.5 eq to 2598.04 kg $PM_{2.5}$ eq. PAN CF offers a more moderate reduction of about 64%, with an impact of 14 132.35 kg $PM_{2.5}$ eq.

The PAN CF electrode reduces terrestrial acidification impact by ≈33%, bringing it down from 106 156.84 kg SO_2 eq to 71 320.78 kg SO_2 eq. Whereas, the lignin CF electrode performs far better, achieving an 88% reduction to 12 419.07 kg SO_2 eq. Freshwater eutrophication decreases by around 10% with PAN CF, while lignin CF shows a 17% reduction. In terms of freshwater ecotoxicity, PAN CF provides a 40% reduction compared to the baseline, lowering the impact from 2.20×10^6 kg 1,4-DCB to 1.33×10^6 kg 1,4-DCB, while lignin CF reduces it by 44%.

Human carcinogenic toxicity is significantly reduced with both alternative electrodes. The PAN CF achieves a 79% decrease, lowering the impact from 6.89×10^6 kg 1,4-DCB in the baseline to 1.45×10^6 kg 1,4-DCB. The lignin CF performs even better, reducing the impact by 81%, 1.31×10^6 kg 1,4-DCB. In terms of fossil resource scarcity, Lignin CF achieves an astounding 98% reduction compared to the baseline, bringing the impact from 3.76×10^6 kg oil eq to just 66689.19 kg oil eq. PAN CF also reduces the impact, but less dramatically, by about 43%, with a final value of 2.13×10^6 kg oil eq.

3.2.4. Key Insights from LCA Analysis

While the seawater-river RED and brine-WWTP RED systems offer an innovative solution for energy generation, significant environmental impacts, particularly in GWP, toxicity categories, and resource scarcity, must be addressed. Future improvements should focus on optimizing materials, reducing energy consumption, and adopting cleaner technologies for membrane production. These optimizations could help the RED system align better with sustainability goals and reduce its overall environmental footprint.

In the scenario analysis for the seawater-river RED system, the comparison across three electrode materials suggests that while both PAN CF and Lignin CF electrodes significantly reduce most environmental impacts, Lignin CF electrodes present the most environmentally beneficial alternative overall, especially in terms of global warming, particulate matter, and resource scarcity. However, the increased impacts related to ozone depletion and freshwater eutrophication should not be overlooked, as they indicate potential areas for further refinement in deploying carbon-based electrodes. In the brine-WWTP RED scenario analysis, Lignin CF consistently outperforms both the baseline and PAN CF electrodes across all the impact categories, with reductions ranging from 17% to as much as 98%. While PAN CF also provides significant improvements, its reductions are generally less pronounced than those of lignin CF. This highlights the

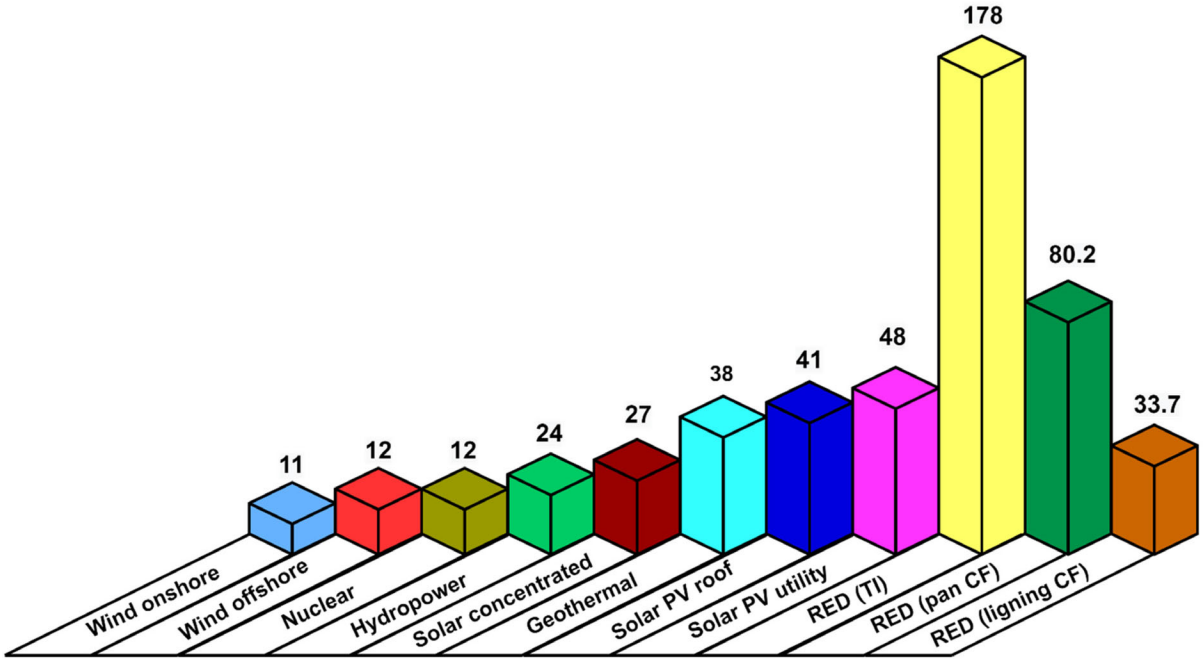

Figure 9. Life-cycle grams CO_2 eq emissions per kWh energy Production.

potential of Lignin CF as a more environmentally sustainable alternative for Brine-WWTP RED systems.

When comparing with other renewable sources, the carbon emission per kWh of energy produced from the seawater-river RED system, especially with the baseline Ti electrode, are still significantly higher at 178 g CO_2 eq/kWh compared to wind, solar PV, and hydropower (see **Figure 9**).[56] However, using carbon fiber electrodes such as PAN CF and Lignin CF notably reduces emissions to 80.15 g CO_2 eq/kWh and 33.73 g CO_2 eq/kWh, respectively. These reductions demonstrate that while RED systems initially have higher emissions than many renewable energy sources, advancements like carbon fiber electrodes can considerably improve their environmental performance.

4. Conclusion

This study applied a full-factorial experimental design to evaluate the key parameters—salinity, flow rate, and temperature of sea and river water—that influence SGP generation using RED, specifically within the seasonal and geographical context of Sweden. To enhance predictive capabilities, ML methods were employed, including 1) EL with DT weak learners, 2) GPR, and a custom-designed 3) ANN. Among these, the custom-designed ANN demonstrated the highest predictive accuracy with an R^2 of 99.35% and an RMSE of 1.173%, closely followed by the GPR model with an R^2 of 99.17% and an RMSE of 1.95%. Feature importance analysis underscored sea salinity as the most influential factor in determining *PD*, followed by temperature, sea flow velocity, and river flow velocity. These findings highlight the complex interplay of environmental factors in optimizing energy generation from salinity gradients and provide a robust framework for further exploration and development of RED technology in diverse settings.

The LCA discovered notable environmental impacts for both the seawater-river RED and brine-WWTP RED systems, with respective GWP of 178 g CO_2 eq/kWh and 158 g CO_2 eq/kWh, largely attributed to energy-intensive Ti electrode production and system pumping requirements. Comparative analysis showed that substituting Ti electrodes with advanced carbon fiber-based options, particularly lignin-derived carbon fiber (CF), significantly reduced GWP by 81%, achieving a GWP as low as 33.73 g CO_2 eq/kWh. This highlights the potential of lignin CF to enhance the sustainability of RED systems. However, challenges remain, as ozone depletion and freshwater eutrophication impacts associated with carbon-based electrodes warrant further investigation into synthesis and material refinement. Despite higher emissions compared to RERs like hydropower, solar PV, and wind, the integration of advanced CF electrodes within seawater-river RED systems demonstrates a promising pathway for enhancing the efficiency and sustainability of blue energy, especially within the context of Swedish energy needs.

Supporting Information

Supporting Information is available from the Wiley Online Library or from the author.

Acknowledgements

Y.M. and M.M. contributed equally to this work. The authors would like to express their appreciation for the financial support of Swedish Energy Agency, Sweden (ref. 51675-1) as well as and the Kempe Foundation (grant no. JCK22-0225) Sweden. The authors appreciated the contribution of Ms. Defne Bilen.

Conflict of Interest

The authors declare no conflict of interest.

Data Availability Statement

The data that support the findings of this study are available in the supplementary material of this article.

Keywords

blue energy in sweden, life cycle assessments, machine learning, power density, reverse electrodialysis, salinity gradient power

Received: April 2, 2025
Revised: May 12, 2025
Published online:

[1] H. Yu, B. Wen, I. Zahidi, M. F. Chow, D. Liang, D. Ø. Madsen, *Results Eng.* **2024**, *22*, 102324.
[2] L. Nouri, G. Mahtabi, S. H. Hosseini, C. V. S. R. Prasad, *Results Eng.* **2024**, *21*, 101871.
[3] L. Nordenstam, *Energy Rep.* **2024**, *11*, 6126.
[4] I. Karakurt, B. D. Avci, G. Aydin, *Environ. Sci. Pollut. Res.* **2024**, *31*, 52448.
[5] M. Rastgar, K. Moradi, C. Burroughs, A. Hemmati, E. Hoek, M. Sadrzadeh, *Chem. Rev.* **2023**, *123*, 10156.
[6] L. Amjith, B. Bavanish, *Chemosphere* **2022**, *293*, 133579.
[7] J. Rani, J. Kumari, S. K. Chand, S. Chand, *Big Data, Artificial Intelligence, and Data Analytics in Climate Change Research*, Springer, Singapore **2024**, pp. 153–171, https://doi.org/10.1007/978-981-97-1685-2_9.
[8] Q. Hassan, S. Algburi, A. Z. Sameen, H. M. Salman, M. Jaszczur, *Results Eng.* **2023**, *20*, 101621.
[9] E. Kabir, P. Kumar, S. Kumar, A. Adelodun, K.-H. Kim, *Renewable Sustainable Energy Rev.* **2017**, *82*, 894.
[10] L. Bird, D. Lew, M. Milligan, E. M. Carlini, A. Estanqueiro, D. Flynn, E. Gomez-Lazaro, H. Holttinen, N. Menemenlis, A. Orths, P. B. Eriksen, J. C. Smith, L. Soder, P. Sorensen, A. Altiparmakis, Y. Yasuda, J. Miller, *Renewable Sustainable Energy Rev.* **2016**, *65*, 577.
[11] W.-S. Hsu, A. Preet, T.-Y. Lin, T.-E. Lin, *Molecules* **2021**, *26*, 5469.
[12] K. Zachopoulos, N. Kokkos, C. Elmasides, G. Sylaios, *Energies* **2022**, *15*, 2970.
[13] O. A. Alvarez-Silva, A. F. Osorio, C. Winter, *Renewable Sustainable Energy Rev.* **2016**, *60*, 1387.
[14] J. Kuleszo, C. Kroeze, J. Post, B. M. Fekete, *J. Integr. Environ. Sci.* **2010**, *7*, 89.
[15] P. Stenzel, H. J. Wagner, in *3rd Int. Conf. Ocean Energy*, Bilbao October **2010**.
[16] F. Helfer, C. Lemckert, Y. G. Anissimov, *J. Memb. Sci.* **2014**, *453*, 337.

[17] J. W. Post, *Blue Energy: Electricity Production from Salinity Gradients by Reverse Electrodialysis*, Wageningen University and Research, Wageningen **2009**.
[18] S. Loeb, R. S. Norman, *Science* **1975**, *189*, 654.
[19] F. Helfer, C. Lemckert, *Renewable Sustainable Energy Rev.* **2015**, *50*, 1.
[20] Y. Berrouche, P. Pillay, *J. Renewable Sustainable Energy* **2012**, *4*, 053113.
[21] S. Lin, Z. Wang, L. Wang, M. Elimelech, *Joule* **2024**, *8*, 334.
[22] European Commission, D.-G. for Maritime Affairs, Fisheries, Blue energy : action needed to deliver on the potential of ocean energy in European seas and oceans by 2020 and beyond : communication from the Commission to the European Parliament, the Council, the European Economic and Social Committee and the Committe, Publications Office **2014**, https://doi.org/10.2771/32703.
[23] C. Simões, M. Saakes, D. Brilman, *Ind. Eng. Chem. Res.* **2023**, *62*, 1665.
[24] J. Kim, K. Jeong, M. J. Park, H. K. Shon, J. H. Kim, *Energies* **2015**, *8*, 11821.
[25] S. Foorginezhad, M. M. Zerafat, Y. Mohammadi, M. Asadnia, *Clean. Eng. Technol.* **2022**, *10*, 100550.
[26] J. Jang, Y. Kang, J.-H. Han, K. Jang, C.-M. Kim, I. S. Kim, *Desalination* **2020**, *491*, 114540.
[27] M. Sharma, P. P. Das, A. Chakraborty, M. K. Purkait, *Sustainable Energy Technol. Assessments* **2022**, *49*, 101687.
[28] K. E. Mueller, J. T. Thomas, J. X. Johnson, J. F. DeCarolis, D. F. Call, *J. Ind. Ecol.* **2021**, *25*, 1194.
[29] C. Li, Z. Zhang, Z. Li, N. Qiao, H. Guo, J. Liao, *Desalination* **2024**, *571*, 117044.
[30] C.(李昌铮) Li, Z.(李振全) Li, Z.(张哲) Zhang, N.(乔楠) Qiao, M.(廖梦振) Liao, *Phys. Fluids* **2024**, *36*, 22007.
[31] C. Tristán, M. Rumayor, A. Dominguez-Ramos, M. Fallanza, R. Ibáñez, I. Ortiz, *Energy Fuels* **2020**, *4*, 4273.
[32] R. A. Tufa, E. Rugiero, D. Chanda, J. Hnàt, W. van baak, J. Veerman, E. Fontananova, G. Di Profio, E. Drioli, K. Bouzek, E. Curcio, *J. Memb. Sci.* **2016**, *514*, 155.
[33] Z. Wang, J. Li, H. Wang, M. Li, L. Wang, X. Kong, *Front. Energy Res.* **2022**, *10*, 919878.
[34] A. Cipollina, G. Micale, *Sustainable Energy from Salinity Gradients*, Elsevier, Amsterdam **2016**.
[35] Y. Mohammadi, S. Mahdi Miraftabzadeh, M. H. J. Bollen, M. Longo, *Int. J. Electr. Power Energy Syst.* **2022**, *143*, 108516.
[36] Y. Mohammadi, S. M. Miraftabzadeh, M. H. J. Bollen, M. Longo, *Sustainable Energy Grids Netw.* **2022**, *31*, 100773.
[37] Y. Mohammadi, B. Polajžer, R. C. Leborgne, D. Khodadad, *Sustainable Energy Grids Netw.* **2024**, *38*, 101359.
[38] Y. Mohammadi, B. Polajžer, R. C. Leborgne, D. Khodadad, *Eng. Appl. Artif. Intell.* **2024**, *133*, 108331.
[39] L. Blakely, M. J. Reno, R. J. Broderick, in *2018 IEEE Power Energy Soc. Innov. Smart Grid Technol. Conf. ISGT 2018*, **2018** pp. 1–5, https://doi.org/10.1109/ISGT.2018.8403323.
[40] J. M. Klusowski, Complete analysis of a random forest model, ArXiv **2018**, *13*, 1063.
[41] A. Natekin, A. Knoll, *Front. Neurorobot.* **2013**, *7*, https://doi.org/10.3389/fnbot.2013.00021.
[42] Y. Mohammadi, A. Salarpour, R. Chouhy Leborgne, *Int. J. Electr. Power Energy Syst.* **2021**, *124*, 106363.
[43] H. Sheng, J. Xiao, Y. Cheng, Q. Ni, S. Wang, *IEEE Trans. Ind. Electron.* **2018**, *65*, 300.
[44] P. M. R. Bento, J. A. N. Pombo, R. P. G. Mendes, M. R. A. Calado, S. J. P. S. Mariano, *Ocean Eng.* **2021**, *219*, 108372.
[45] S. S. Madaeni, N. T. Hasankiadeh, A. R. Kurdian, A. Rahimpour, *Sep. Purif. Technol.* **2010**, *76*, 33.
[46] Y. Mohammadi, S. M. Miraftabzadeh, M. H. J. Bollen, M. Longo, *Sustainable Energy Grids Netw.* **2022**, *32*, 100855.
[47] Y. Zhu, B. Lian, Y. Wang, C. Miller, C. Bales, J. Fletcher, L. Yao, T. D. Waite, *Water Res.* **2022**, *227*, 119349.
[48] S. Waugh, Extending and benchmarking cascade-correlation, Department of Computer Science at the University of Tasmania, Ph.D. Dissertation **1995**.
[49] S. M. Rahman, M. J. Eckelman, A. Onnis-Hayden, A. Z. Gu, *Environ. Sci. Technol.* **2018**, *52*, 11346.
[50] R. A. Tufa, E. Curcio, E. Brauns, W. van Baak, E. Fontananova, G. Di Profio, *J. Memb. Sci.* **2015**, *496*, 325.
[51] A. Daniilidis, R. Herber, D. A. Vermaas, *Appl. Energy* **2014**, *119*, 257.
[52] M. Huijbregts, Z. Steinmann, P. Elshout, G. Stam, F. Verones, M. Vieira, M. Zijp, A. Hollander, R. Zelm, *Int. J. Life Cycle Assess.* **2016**, *22*, 138.
[53] M. H. Kjell, E. Jacques, D. Zenkert, M. Behm, G. Lindbergh, *J. Electrochem. Soc.* **2011**, *158*, A1455.
[54] W. Qu, P. Hu, J. Liu, H. Jin, K. Wang, *J. Clean. Prod.* **2022**, *343*, 131030.
[55] B. V. Surya Vardhan, M. Khedkar, I. Srivastava, S. K. Patro, *Electr. Power Syst. Res.* **2024**, *230*, 110222.
[56] Intergovernmental Panel on Climate Change, *Climate Change 2014: Mitigation of Climate Change*, Cambridge University Press, Cambridge **2015**, pp. 1329–1356, https://doi.org/10.1017/CBO9781107415416.025
[57] R. A. Tufa, S. Pawlowski, J. Veerman, K. Bouzek, E. Fontananova, G. di Profio, S. Velizarov, J. Goulão Crespo, K. Nijmeijer, E. Curcio, *Appl. Energy* **2018**, *225*, 290.